

Fully packed quantum loop model on the triangular lattice: Hidden vison plaquette phase and cubic phase transitions

Zheng Yan,^{1, 2, *} Xiaoxue Ran,^{1, *} Yan-Cheng Wang,³ Rhine Samajdar,⁴ Junchen Rong,⁵ Subir Sachdev,^{4, 6} Yang Qi,^{2, 7, 8, †} and Zi Yang Meng^{1, ‡}

¹*Department of Physics and HKU-UCAS Joint Institute of Theoretical and Computational Physics, The University of Hong Kong, Pokfulam Road, Hong Kong SAR, China*

²*State Key Laboratory of Surface Physics, Fudan University, Shanghai 200433, China*

³*School of Materials Science and Physics, China University of Mining and Technology, Xuzhou 221116, China*

⁴*Department of Physics, Harvard University, Cambridge, MA 02138, USA*

⁵*Institut des Hautes Études Scientifiques, 91440 Bures-sur-Yvette, France*

⁶*School of Natural Sciences, Institute for Advanced Study, Princeton, NJ 08540, USA*

⁷*Center for Field Theory and Particle Physics, Department of Physics, Fudan University, Shanghai 200433, China*

⁸*Collaborative Innovation Center of Advanced Microstructures, Nanjing 210093, China*

(Dated: May 11, 2022)

Quantum loop and dimer models are prototypical correlated systems with local constraints, whose generic solutions for different lattice geometries and parameter regimes are still missing due to the lack of controlled methods to solve such systems in the thermodynamic limit. Here, we obtain, via the newly developed sweeping cluster quantum Monte Carlo algorithm, the phase diagram of the triangular-lattice fully packed quantum loop model (quantum dimer model with two dimers per site). We find that as the interaction turns from attractive to repulsive, the system has a first-order transition from a lattice nematic (LN) solid to a novel vison plaquette (VP) solid without dimer density modulations but with off-diagonal order. Further increasing the dimer repulsion towards the Rokhsar-Kivelson point, the VP phase experiences a continuous transition to an even \mathbb{Z}_2 quantum spin liquid (QSL) phase. Our results reveal the LN-to-VP first-order transition is triggered by the intricate change from face- to corner-cubic anisotropy of the $O(3)$ vison order parameter, and the VP-to-QSL continuous transition is of the cubic universality class, which is very close to the $(2+1)D$ $O(3)$ one, in full consistency with the recent conformal bootstrap findings on the cubic fixed point.

Introduction.—In quantum many-body systems, topologically ordered phases [1–4] and their fractionalized excitations [2, 5] have attracted much attention because they hold the promise of providing solutions to many mysteries of highly entangled quantum matter such as unconventional superconductors [6–8], quantum moiré materials [9, 10], frustrated quantum magnets [11–18], and—more recently—programmable Rydberg quantum simulators [19–23]. Concomitantly, the quantum phase transitions between topologically ordered phases and conventional symmetry-breaking states have also been actively investigated with a variety of theoretical and numerical approaches [22–32].

One of the widely studied models to realize such phase transitions is the quantum dimer model (QDM) [6, 8]. In QDMs, \mathbb{Z}_2 topologically ordered phases originate from the famous Rokhsar-Kivelson (RK) point [3, 8, 33–36] and acquire extended phase space on nonbipartite triangular and kagome lattices [32, 34, 35, 37–39]. However, away from the RK point, the overall structures of the phase diagrams on various 2D geometries—either bipartite or nonbipartite—such as square and triangular lattices, are still under intensive investigation [26, 27, 32, 40–43]. This is due to both the lack of controlled

methodology to solve these strongly correlated lattice models with local constraints and new discoveries that either confirm or defy earlier nonrigorous arguments.

In this paper, we study a QDM on a triangular lattice where two dimers touch every lattice site, which is also dubbed the fully packed quantum loop model (QLM) [27, 45–47]; we will mainly use this notation for the sake of simplicity. In the strongly interacting limit, the QLM shares the Hilbert space and low-energy properties of the hard-core boson model (or spin-1/2 XXZ model) on a kagome lattice at 1/3 filling and many other similar frustrated models with local constraints [27, 28, 48, 49]. The QLM is also related to the resonant-valence-loop phase in frustrated spin-1 models [50, 51], analogously to the relation between the one-dimer-per-site QDM and spin- $\frac{1}{2}$ models. The triangular-lattice QLM has been investigated by field-theoretical analyses and various numerical approaches [26, 27], but, so far, no consistent phase diagram has been obtained.

We now summarize the overall understanding of the phase diagram before the present work. At the RK point, the model realizes a \mathbb{Z}_2 quantum spin liquid (QSL) phase, which has even \mathbb{Z}_2 topological order and hosts fractionalized quasiparticles called “visons”. Tuning away from the RK point, the model realizes various topologically trivial symmetry-breaking phases. The transitions from the QSL to the topologically trivial phases can be understood as condensation of the visons. Previous numerical studies [26, 27] show that decreasing the repulsion

* These authors contributed equally to this work.

† qiyang@fudan.edu.cn

‡ zymeng@hku.hk

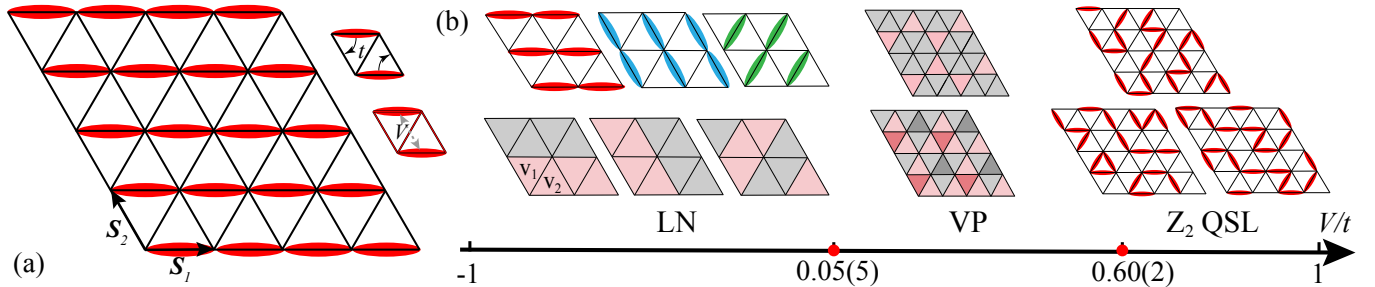


FIG. 1. **Fully packed quantum loop model on the triangular lattice.** (a) Schematic representation of the QLM; s_1 and s_2 are the primitive vectors. The t and V terms in the Hamiltonian Eq. (1) are depicted in the upper-right insets. The dimer configuration sketched is one of the three LN patterns, with fully packed loops along the s_1 direction. (b) Phase diagram of the QLM obtained from our simulations. The first row of the left subfigure illustrates the three LN dimer configurations, corresponding to the three vison patterns shown on the second row. The triangles v_1 and v_2 represent two sublattices for the visons, and the red and grey colors in the triangles denote vison numbers (± 1) with opposite sign. The first-order phase transition between the LN and VP states occurs at $V = 0.05(5)$. The first row of the middle subfigure is the kinetic energy correlation pattern and the second row is the vison plaquette (VP) pattern based on QMC simulation results, respectively (see Fig. S3(a) and (b) in the SM [44]). VP is a *hidden* dimer solid phase without dimer order. The right subfigures are the representative dimer coverings in the \mathbb{Z}_2 QSL phase. The continuous phase transition between the VP phase and the QSL occurs at $V_c = 0.60(2)$.

between parallel dimers leads to a lattice nematic (LN) solid phase. Furthermore, the phase transition between the QSL and the LN phase, described by vison condensation, is suggested to have an emergent $O(3)$ symmetry and therefore, belongs to the 3D $O(3)$ universality class. These two works employ different methods, namely, exact diagonalization (ED) of small systems and density-matrix renormalization group (DMRG) calculations [26], or variational quantum Monte Carlo (QMC) simulations at intermediate system sizes of 12×12 [27]. Importantly, the numerical evidence presented in these two works disagree on the boundary of the phase diagram. In particular, the former indicates that the LN–QSL transition occurs at $V/t \sim -0.3$ whereas the latter estimated this point to be at $V/t \sim 0.7$ and found the LN order is vanishingly small between $V/t \in (-0.3, 0.7)$.

Theoretically, the speculation of the LN–QSL transition being in the $O(3)$ universality class is based on the *assumption* that the cubic anisotropy is irrelevant at the 3D $O(3)$ Wilson-Fisher fixed point [52–56]. However, this assumption has been disproven by recent conformal bootstrap analyses [57] demonstrating that the 3D $O(3)$ fixed point is unstable and will flow towards the nearby “corner cubic” fixed point, whose symmetry breaking phase is the corner cubic phase. Moreover, a previous study [48] on the honeycomb-lattice transverse-field Ising model (which is related to the current QLM by approximating the vison excitation with Ising spins) shows a first-order transition instead of a continuous one, with clear face-centered cubic anisotropy at the transition point. Therefore, resolving the controversy in the phase diagram of the triangular-lattice QLM requires a new and consistent understanding that unifies the aforementioned recent developments [26, 27, 48, 57], and provides as well the correct mechanism of the vison condensation transition from the \mathbb{Z}_2 QSL to solid phases [58].

These are the questions addressed in this work. Employing the sweeping cluster quantum Monte Carlo method [22, 32, 43, 59, 60], we explore the ground-state phase diagram of the triangular-lattice QLM in an unbiased manner. We find, using both QMC and ED analyses, that between the proposed LN phase [61] and the \mathbb{Z}_2 QSL phase, there exists a new “vison plaquette” (VP) solid state, which has no apparent dimer order. The phase transition between the LN and VP phases is first-order, and that from the VP to the \mathbb{Z}_2 QSL phase is continuous. The VP phase resides exactly in the region where the previous work [27] found the vanishingly small LN order (but did not probe the VP order parameter). More interestingly, our numerical discoveries of the LN–VP first-order transition and the VP–QSL continuous transition provide a unified understanding that is fully consistent with the recent conformal bootstrap analysis of the relation between the $O(3)$ and cubic fixed points in $(2+1)D$ [57], which on its own has a long and rich history [52–56]. Therefore, it is of general interest to the condensed matter, statistical physics, quantum simulation, and field theoretical communities that our results for the QLM on the triangular lattice provide the first nontrivial realization of this profound scenario in a setting that is potentially experimentally accessible in programmable quantum simulators based on highly tunable Rydberg atom arrays [22, 62–66] (in which each dimer can be identified with an atom excited to a Rydberg state by laser pumping [19, 20]).

Model and methods.—The Hamiltonian of the quantum loop model on a triangular lattice is defined as

$$H = -t \sum_{\alpha} \left(\left| \begin{array}{c} \diagup \\ \diagdown \end{array} \right\rangle \left\langle \begin{array}{c} \diagdown \\ \diagup \end{array} \right| + h.c. \right) + V \sum_{\alpha} \left(\left| \begin{array}{c} \diagup \\ \diagdown \end{array} \right\rangle \left\langle \begin{array}{c} \diagdown \\ \diagup \end{array} \right| + \left| \begin{array}{c} \diagdown \\ \diagup \end{array} \right\rangle \left\langle \begin{array}{c} \diagup \\ \diagdown \end{array} \right| \right), \quad (1)$$

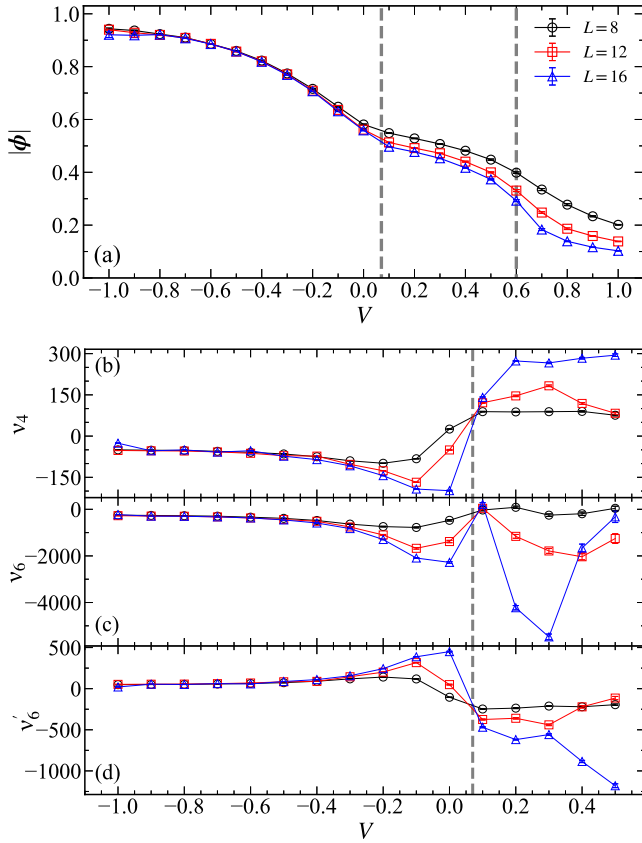


FIG. 2. Quantum phase transitions in the triangular lattice QLM. (a) Vison O(3) order parameter $|\phi|$ as a function of V . The two dashed lines are guides to the eye for the position of the LN–VP first-order transition and the VP–QSL continuous transition. Panels (b), (c), and (d) show the coefficient of the anisotropies ν_4 , ν_6 , and ν'_6 in the effective action (3), computed from the QMC histogram data in Fig. 3 of the O(3) order parameter. ν_4 changes sign at the LN–VP transition (at the position of the dashed line), signifying the face- to corner-cubic anisotropy in the effective action of the lattice model.

where α represents the three possible orientations of all plaquettes of the triangular lattice, as shown in Fig. 1(a) for an example of the LN state. The local constraint of our model requires two dimers to touch every triangular-lattice site in any configuration, therefore forming the fully packed quantum loops [27]. The kinetic term is controlled by t , which changes the dimer covering of every flippable plaquette while respecting the local constraint, and V is the repulsion ($V > 0$) or attraction ($V < 0$) between dimers facing each other. The special RK point is located at $t = V$ and has an exact \mathbb{Z}_2 QSL solution [34]. We set $t = 1$ as the unit of energy in our simulations.

We employ the recently developed powerful sweeping cluster quantum Monte Carlo method [32, 59, 60] to solve this model. Our simulations are performed on the triangular lattice with periodic boundary conditions and system sizes $N = 3L^2$ for linear dimensions $L = 8, 12$ and 16 , while setting the the inverse temperature $\beta = L$.

Further description of the QMC implementation and its advantages can be found in the Supplementary Material (SM) [44].

Physical observables.—To explore the phase diagram of the Hamiltonian in Eq. (1), we first measure the order parameter describing the soft vison modes [26, 67–69], which is given by

$$\phi_j = \sum_{\mathbf{r}} (v_{1,\mathbf{r}}, v_{2,\mathbf{r}}) \cdot \mathbf{u}_j e^{i\mathbf{M}_j \cdot \mathbf{r}}, \quad j = 1, 2, 3, \quad (2)$$

where \mathbf{r} runs over all the unit cells on the triangular lattice, as shown in Fig. 1(a). The vector $\phi = (\phi_1, \phi_2, \phi_3)$ encapsulates the O(3) order parameters of the visons, which are obtained from the Fourier transforms of vison configurations $v_i v_j = (-1)^{N_{P_{ij}}}$, with $N_{P_{ij}}$ being the number of dimers cut along the path P between triangular plaquettes i and j [32]. The label $(v_{1,\mathbf{r}}, v_{2,\mathbf{r}})$ denotes visons living in the centres of the two sublattices of the triangle plaquette at \mathbf{r} [see the left subfigure in Fig. 1(b)]. In our simulation, we choose a reference vison on a certain triangular plaquette, e.g., by setting $v_{1,\mathbf{r}=(0,0)} = \pm 1$ on the upper triangle of the first unit cell. The vison configurations are obtained with respect to such a reference, from which we can assign values of $(v_{1,\mathbf{r}}, v_{2,\mathbf{r}})$ for all \mathbf{r} . The three momenta $\mathbf{M}_1 = (\pi/\sqrt{3}, \pi/3)$, $\mathbf{M}_2 = (\pi/\sqrt{3}, -\pi/3)$, and $\mathbf{M}_3 = (0, 2\pi/3)$ correspond to the low-energy modes of the vison dispersion and are invariant under the projective symmetry transformations [26, 44, 69]. The associated \mathbf{u}_j are $(1, 1)^T$ for \mathbf{M}_1 and \mathbf{M}_2 , and $(1, -1)^T$ for \mathbf{M}_3 . The derivation of Eq. (2), the symmetry analysis of the vison O(3) order parameter, and representative vison configurations in the VP phase are presented in the SM [44].

The vector (ϕ_1, ϕ_2, ϕ_3) can also describe the vison condensation transition [26, 48]. We take the magnitude $|\phi| = \sqrt{\phi_1^2 + \phi_2^2 + \phi_3^2}$, plotted in Fig. 2(a), as the order parameter to detect the solid phases and their transitions to the \mathbb{Z}_2 QSL phase. As illustrated in Fig. 2(a), the $|\phi|$ order parameter clearly develops a two-step vanishing process with increasing system sizes. When $V < 0$, the order parameter is finite, denoting the long-range order in the vison pattern and the LN phase, shown in the left subfigure in Fig. 1(b); when $V > 0$, ϕ drops to a finite plateau, signifying another symmetry-breaking phase.

To further reveal the nature of the symmetry-breaking phases, we plot the histogram of the order parameter ϕ in Fig. 3. The distribution of ϕ is indeed different in the two phases: it is peaked at the six face centres of the cube in the phase for $V < 0$, and at the eight corners of the cube in the phase for $0 < V < 0.6$. According to the symmetry transformation of ϕ (see SM [44]), a peak at the face centre breaks threefold rotational symmetry while preserving translational and twofold rotational symmetries. From the broken symmetries, we recognise that this is the LN phase. On the other hand, a peak at the corner breaks the translational symmetry in a manner that doubles the unit cell in both directions, while preserving

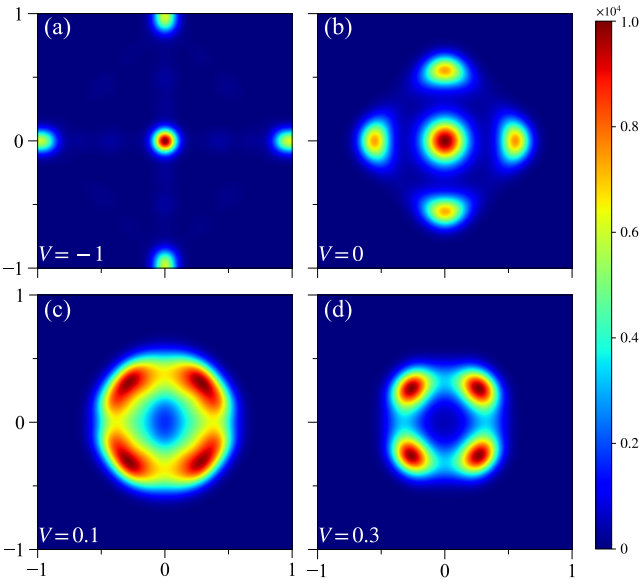


FIG. 3. Histograms of the $O(3)$ order parameter. These histograms are plotted on the two-dimensional (ϕ_1, ϕ_2) plane and are obtained from the QMC data of $L = 16$ systems with different V . The (a,b) face-cubic anisotropies inside the LN phase, where the coefficient $\nu_4 < 0$ in Fig. 2(b), and the (c,d) corner-cubic anisotropies inside the VP phase, where $\nu_4 > 0$ in Fig. 2(b), are manifest.

the rotational symmetries. Therefore, the ground state is a plaquette-ordered phase with a 2×2 unit cell. As we will discuss later, the ground state does not exhibit any symmetry breaking in the dimer-dimer correlations but does so in other correlation functions; hence, we refer to it as the vison plaquette phase.

The phase transition between the LN and VP phases at $V \sim 0$, denoted by the left grey dashed line in Fig. 2(a), is first-order, which is expected because they break incompatible symmetries. The vison condensation transition between the VP phase and the \mathbb{Z}_2 QSL happens at $V \sim 0.6$, as indicated by the right grey dashed line in Fig. 2(a), and it appears to be continuous. The natures of the two transitions will be studied in more detail below.

Effective action and renormalization-group analysis.—In order to fully understand the LN–VP first-order transition and the VP–QSL continuous transition, as well as their fundamental relation to the $O(3)$ and cubic fixed points in $(2+1)D$, we will need to first explain the effective action and the renormalization-group (RG) analysis of the problem in a more general and up-to-date setting. The low-energy description of these transitions, with the $O(3)$ order parameter ϕ in Eq. (2), can be cast into the action [26] $S = \int dt d^2x L$ with the Lagrangian

$$L = \sum_{i=1}^3 (\partial_\mu \phi_i)^2 + r \sum_{i=1}^3 \phi_i^2 + \mu (\sum_{i=1}^3 \phi_i \phi_i)^2 + \nu_4 \sum_{i=1}^3 (\phi_i)^4,$$

$$+ \mu_6 (\sum_{i=1}^3 \phi_i^2)^3 + \nu_6 (\phi_1 \phi_2 \phi_3)^2 + \nu'_6 (\sum_{i=1}^3 \phi_i^2) (\sum_{i=1}^3 \phi_i^4), \quad (3)$$

coupled to a \mathbb{Z}_2 gauge theory. The \mathbb{Z}_2 gauge theory does not change the dynamics of the system; its effect is to gauge out operators that are odd under the \mathbb{Z}_2 symmetry which flip the sign of all three ϕ_i fields. The first three terms and the μ_6 terms in Eq. (3) preserve the $O(3)$ symmetry. The ν_4 , ν_4 and ν'_6 terms, on the other hand, break the symmetry down to $(\mathbb{Z}_2)^2 \rtimes S_3 = Z_2 \times S_4$. The resultant group is sometimes referred as the “cubic group”, since it is the symmetry group of a three-dimensional cube. This cubic model has a long history (for a review see Ref. 56) since its first appearance in describing the structural phase transition of perovskites [52, 55]. More recently, the structural phase transition of single layer transition metal dichalcogenides, such as MoS_2 , was observed experimentally [70–72], and this can also be described by the effective action above [73].

Mean-field theory suggests that when $\nu_4 > 0$, in the symmetry-broken phase ($r < 0$), the minima of the effective potential are located at

$$\langle \phi_1 \rangle = \pm v, \quad \langle \phi_2 \rangle = \pm v, \quad \langle \phi_3 \rangle = \pm v. \quad (4)$$

Such a phase is commonly called the “corner-cubic” phase, corresponding to the bright spots in the histograms in Figs. 3(c) and (d); here, the eight possible states are in one-to-one correspondence with the eight vertices of a three-dimensional cube. When $\nu_4 < 0$, the symmetry-broken phase is described by

$$\langle \phi_1 \rangle = \pm v', \quad \langle \phi_2 \rangle = \langle \phi_3 \rangle = 0, \quad (5)$$

together with the other states where either $\langle \phi_2 \rangle$ or $\langle \phi_3 \rangle$ acquires an expectation value. The six symmetry-broken states in this case correspond to the face centers of a three-dimensional cube, thus defining a “face-cubic” phase [bright spots in the histograms in Figs. 3(a) and (b)], which has also been seen in the honeycomb-lattice transverse-field Ising model [48] that bears a low-energy action similar to Eq. (3).

Studying the RG flow suggests that when $\nu_4 > 0$, the theory (3) flows to a conformal field theory. This tells us that the phase transition from the disordered phase to the corner-cubic phase is second-order and continuous. The RG flows starting from the $\nu_4 < 0$ region, on the other hand, have no fixed point, so the transition from the disordered to the face-cubic phase is first-order. (Strictly speaking, it is possible for the attractor basin of the conformal fixed point to cover a small portion of the region with $\nu_4 < 0$. This, however, is ruled out by more sophisticated analyses, which we will mention later.)

It remains to answer the question to which universality class the $\nu_4 > 0$ phase transition belongs. This seemingly easy question was under debate for many years; see Ref. 55 for a review of early theoretical studies. It was not until much later that a convergent answer was obtained

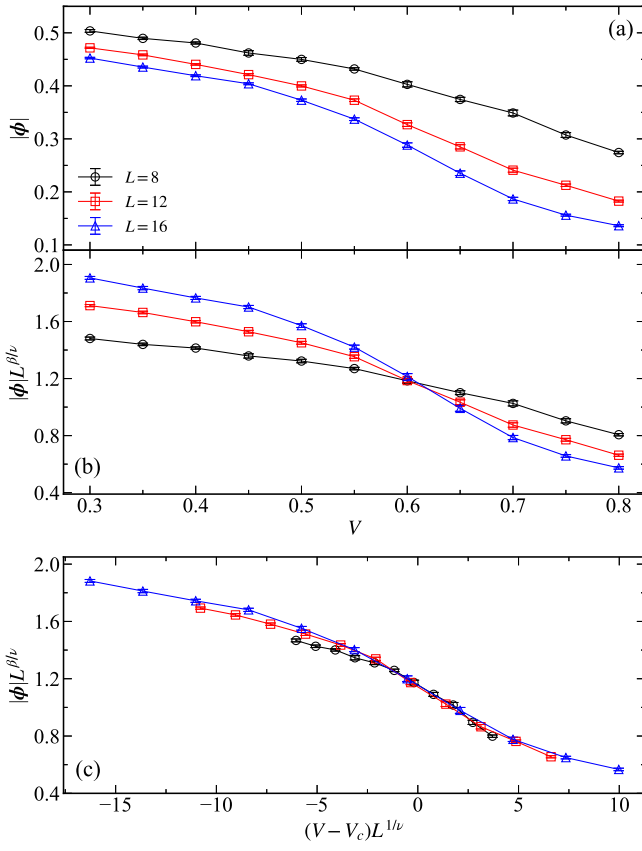


FIG. 4. The cubic fixed point. (a) Vison O(3) order parameter $|\phi|$ across the VP–QSL phase transition for different system sizes. (b) Employing the (2+1)D O(3) critical exponents $\beta = 0.3689(3)$, $\nu = 0.7112(5)$ [76] to rescale the y -axis as $L^{\beta/\nu} \phi$ against V , it is clear that the continuous phase transition manifests as the crossing point between different system sizes at $V_c = 0.60(2)$. (c) With the obtained V_c , one can further rescale the x -axis as $(V - V_c)L^{1/\nu}$, data collapse with O(3) exponents can be clearly seen. We note the difference in critical exponents between the O(3) and cubic fixed points is beyond the resolution at our system sizes and parameter steps.

using three different methods: lattice Monte Carlo simulations [53], perturbative field-theory calculations [54], and the conformal bootstrap [57]. It turns out that the continuous phase transition at $\nu_4 > 0$ is in a new universality class which is different from the O(3)-invariant Heisenberg model. The question of the universality class is closely related to the scaling dimension of the cubic anisotropy operator $O = \sum_{i=1}^3 (\phi_i)^4$. Among the above-mentioned methods, the conformal bootstrap approach [74, 75] provides a concrete nonperturbative proof that $\Delta_O < 3$ [57]. This indicates that the O(3) conformal fixed point is unstable against cubic anisotropy, and therefore, the phase transition should be in a new universal class. We denote the corresponding CFT the “cubic fixed point”.

QMC observation of the RG flow.—With the above back-

ground, we now move back to the QMC data in Figs. 2, 3, and 4.

It is important to notice that at the cubic fixed point, the coupling constant ν_4 is a small positive number. This leaves space for another weakly first-order phase transition when ν_4 changes sign. This is precisely the transition between the corner- and face-cubic phases that we observed at $V/t \approx 0.05$ in the vison order parameter histograms in Fig. 3.

To quantitatively describe the phase transition between the LN and VP phases, we consider the anisotropy parameters ν_4 , ν_6 , and ν'_6 in Eq. (3). In the Monte Carlo simulations, they can be expressed as [48] (see derivations in SM [44])

$$\nu_4 = -\frac{15\sqrt{\pi}}{\langle \phi^4 \rangle} \left(\langle Y_4^0 \rangle + \frac{\langle \phi^2 Y_4^0 \rangle \langle \phi^4 \rangle \langle \phi^6 \rangle - \langle Y_4^0 \rangle \langle \phi^6 \rangle^2}{\langle \phi^6 \rangle^2 - \langle \phi^4 \rangle \langle \phi^8 \rangle} \right), \quad (6)$$

$$\nu_6 = -\frac{231\sqrt{13\pi}}{\langle \phi^6 \rangle} \langle Y_6^0 \rangle, \quad (7)$$

$$\nu'_6 = 15\sqrt{\pi} \left(\frac{\langle \phi^2 Y_4^0 \rangle \langle \phi^4 \rangle - \langle Y_4^0 \rangle \langle \phi^6 \rangle}{\langle \phi^6 \rangle^2 - \langle \phi^4 \rangle \langle \phi^8 \rangle} + \frac{7\sqrt{13}}{10\langle \phi^6 \rangle} \langle Y_6^0 \rangle \right), \quad (8)$$

where Y_4^0 and Y_6^0 are two spherical harmonics given by $Y_4^0 = 3(3 - 30 \cos^2 \theta + 35 \cos^4 \theta)/(16\sqrt{\pi})$, $Y_6^0 = \sqrt{13}(-5 + 105 \cos^2 \theta - 315 \cos^4 \theta + 231 \cos^6 \theta)/(32\sqrt{\pi})$, and θ is the polar angle of the order parameter $\phi = (\phi_1, \phi_2, \phi_3)$ which is defined in Eq. (2) for every component. As shown in Figs. 2(b), (c) and (d), the sign of the anisotropy parameter ν_4 (ν'_6) changes from negative to positive (positive to negative) near the LN–VP transition, whereas ν_6 remains negative and only becomes zero at the first-order transition point. We note that similar approximate emergent continuous symmetry at a first-order transition has been reported in the checkerboard J - Q model in both 2D and 3D lattices [77, 78], where the latter is in fact related to ongoing experimental efforts in understanding the thermodynamic data of the Shastry-Sutherland material $\text{SrCu}_2(\text{BO}_3)_2$ under high pressure [79–81].

Figure 4 shows the critical behavior of the VP–QSL phase transition. From the plot of the vison order parameter $|\phi|$ versus V in Fig. 4(a) for different system sizes, the transition is clearly continuous, and according to the discussion above, this transition belongs to the universality of the cubic fixed point. However, the critical exponents of the cubic fixed point and those of the O(3) fixed point are not separable in the practical terms of the resolution in our study (the scaling dimension of cubic anisotropy is only ~ 0.01 away from 3 [57]). Therefore, in Fig. 4(b), we employed the (2+1)D O(3) β and ν to rescale the order parameter to find the crossing points between different sizes, which yields $V_c = 0.60(2)$. Furthermore, in Fig. 4(c), we rescale the x -axis as $(V - V_c)L^{1/\nu}$ such that a high-quality data collapse is obtained. These analyses firmly establish the fact that the QLM in Eq. (1) completely realizes different limits of the effective action in

Eq. (3) and are consistent with the latest understanding of the fixed points of cubic symmetry.

Hidden order in the vison plaquette phase.—Unlike the translational symmetry breaking revealed by the vison order parameter histogram in Fig. 3, we do not find a corresponding dimer order in the VP phase. In this sense, the VP is a *hidden* order in the dimer basis, which is probably the reason why it went undetected in previous works [26, 27]. To further verify this hidden order in the VP phase, we performed the following analysis.

First, as there is no clear peak in the structure factor of dimer correlations in the VP phase for all the system sizes simulated, we seek help from the vison histograms to amplify any signals of possible symmetry-breaking phases in the dimer patterns. In the VP phase, the eight cubic fixed points stay in eight octants in the histograms [such as in Figs. 3(c) and (d)], so every vison configuration can be classified into a certain octant except those on the boundaries; since two vison classes in opposite octants correspond to the same dimer configuration, there are only four classes of dimer configurations. We classify QMC dimer configurations into these four classes and average the ones in the same class (which would amplify the symmetry breaking in the dimers, if there is any) to obtain the dimer density on the strongest vison-ordered configurations. We collected about 500,000 (300,000) such configurations for $L = 4$ ($L = 8$) system at $V = 0.4$ but found that the real-space dimer density is homogeneous, $\sim 1/3$, on all the bonds of the lattice.

Furthermore, as shown in Fig. S4 and Sec. VI of the SM [44], a similar analysis using the ground-state wavefunction from exact diagonalization (ED) of a 4×4 lattice at $V = 0.3$, which eliminates the statistical error in QMC simulations, also confirms no translational symmetry breaking in the dimer density distribution. Therefore, despite evidence of translational symmetry breaking in Fig. 3, both QMC and ED results strongly suggest that the VP order is a *hidden* order phase in the dimer basis, with a homogeneous dimer occupation. We note that such a unique hidden symmetry-breaking phase has not been reported before in the QDM literature. Whether there are intricate (emergent) symmetries that actually protects the homogeneity is an interesting question for future investigation.

In fact, from the real-space vison correlation function in Fig. S3(b) of the SM [44], the difference in correlation functions between two closest triangles is seen to be a constant (about 0.14 at $V = 0.3$). It is well known that this difference can be translated to the dimer occupation on the bond separating the two neighboring triangles [82]. Thus, the constant vison difference also points to a uniform dimer occupation. It is worth noting that a homogeneous dimer density only requires a constant difference of closest visons instead of a constant vison density. This gives rise to the possibility that this VP order exists separately from the QSL.

On the other hand, we notice that the translational symmetry breaking indicated by the histogram in

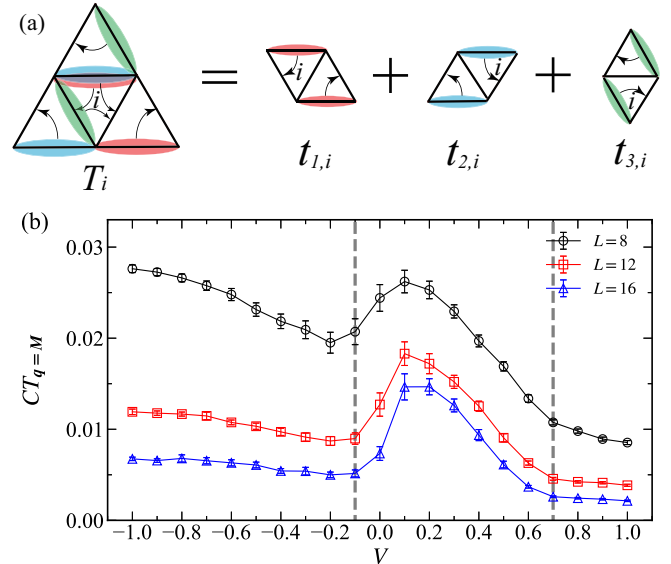


FIG. 5. **Hidden order in the VP phase.** (a) The definition of the operator T_i acting on triangle i . The T_i contain the t -terms of the Hamiltonian (1) on the three rhombi with labels 1, 2, 3 enclosing the triangle i . (b) The structure factor at the M point, $CT_{q=M}$, as a function of V ; in the VP phase, $CT_{q=M}$ acquires long-range order.

Fig. 3(c,d) is indeed reflected in other correlation functions. Firstly, this can be seen from the vison correlations $\langle v_i v_j \rangle$, as displayed in the phase diagram in Fig. 1 and discussed in detail in Sec. III of the SM [44]. We notice that although the vison correlation function appears to change sign under mirror-reflection and sixfold rotations, the physical state actually preserves these symmetries, because of the two-to-one correspondence between vison and dimer configurations. Furthermore, the translational symmetry breaking can also be revealed from correlation functions of local operators.

To see this, we construct the following composite order parameter:

$$T_i = t_{1,i} + t_{2,i} + t_{3,i}, \quad (9)$$

where the sum goes over the t -terms of the Hamiltonian on three rhombi with labels 1, 2, 3 containing the triangle i [Fig. 5(a)]. This is a natural choice of a composite order parameter because it preserves the threefold rotational symmetry. The correlation function of $CT \equiv \langle T_i T_j \rangle$ shows a structure-factor peak at the M point of momentum space in the VP phase as shown in Fig. 5(b). The corresponding real-space CT correlation function—plotted in Fig. S3(a) and sketched in the middle subfigure of Fig. 1(b)—clearly reveals the pattern of translational symmetry breaking and the associated 2×2 unit cell. We can also try to identify $CT_{q=M}$ with operators of the low-energy effective action (3). The operator should break translational symmetry while preserving the sixfold rotational symmetry. Since $CT_{q=M}$ is constructed from dimers in Eq. (9), it should also

be gauge invariant. The natural candidate is therefore $X = \phi_1\phi_2 + \phi_2\phi_3 - \phi_3\phi_1$, which is clearly invariant under the sixfold rotation operation defined in Eq. (S9). After this identification, we can infer the critical behavior of $CT_{\mathbf{q}=\mathbf{M}}$ near the second-order phase transition at $V \sim 0.6$ based on the knowledge of the scaling dimension of X of the cubic CFT. As mentioned already, the cubic CFT and the O(3) CFT have similar critical exponents, since X belongs to the $j = 2$ representation of O(3) (the “T” representation in the notation of Ref. 57), so we obtain the critical exponent $\eta_* \approx 1.42$ [53, 57], which is close to the exponent for the O(2)^{*} transitions observed before [29].

It is interesting to note that this hidden order bears significant implications for the experimental identification of \mathbb{Z}_2 QSLs in Rydberg atom arrays. In recent works [20–22], a “diagonal string operator” has been used to detect the \mathbb{Z}_2 QSL phase in a model of Rydberg atoms with emergent gauge-charged Ising matter degrees of freedom [23]; this operator is defined as an arbitrary closed string that goes across several bond centres, i.e., $Z = (-1)^{\# \text{ cut dimers}}$. While our model has no Ising matter, such a string operator will have a nonzero expectation value in the VP phase as well, *even though* it has no topological order but only a hidden translational symmetry breaking. Therefore, it will be interesting to study the analogs of such VP string order parameters in the Rydberg platform.

Discussion.—Via the newly developed sweeping cluster QMC algorithm, supplemented with ED and symmetry analysis of the vison order parameter, we mapped out the entire phase diagram of the triangular-lattice QLM in an unbiased manner. Our results reveal that the LN–VP first-order transition is triggered by the change from face-to corner-cubic anisotropy of the O(3) vison order parameter, and the VP–QSL continuous transition, driven by the condensation of visons, is of the cubic universality class—which is very close to the (2 + 1)D O(3) one—in full consistency with recent conformal bootstrap findings on the cubic fixed point [57].

The VP solid phase discovered here, has clear translational symmetry breaking in the vison correlation functions and in the dimer hopping order in Fig. 5, but no apparent dimer density order from our ED and QMC simulations. It represents a new state of quantum matter and, at the same time, resolves the previous controversy

in the phase boundaries between the QSL and LN phases in Refs. 26 and 27 (we note that Ref. 27 had in fact observed evidence of the vanishing dimer order parameter in this phase in a parameter regime consistent with ours).

In light of the recent experiments with programmable quantum simulators based on highly tunable Rydberg atom arrays, our results could also have direct experimental relevance. The experiment in Refs. [21] are for the case where the atoms are positioned on the *links* of the kagome lattice, connecting to the quantum dimer model on the kagome lattice [20]. Our study on the triangular-lattice quantum loop model connects to the case where the atoms are placed on the *sites* of the kagome lattice [19]. Investigation of the LN, hidden-order VP, and \mathbb{Z}_2 QSL phases—as well as their subtle phase transitions in the context of the O(3) versus cubic fixed points—can inspire new experiments. In particular, for the case with Rydberg atoms on the kagome sites, an analog of the VP order is a promising possibility for the region proximate to the so-called “string” phase identified in Fig. 1(e) of Ref. 19. Finally, the interplay between the VP and QSL phases could also be relevant to related numerical and theoretical studies of this system [22, 23].

Acknowledgements—We thank Ning Su for insightful discussions on the O(3) and cubic fixed points, and thank Subhro Bhattacharjee, Frank Pollmann, Fabian Alet, and Sylvain Capponi for valuable discussions on the phase diagram of the QLM over the years. XXR, ZY and ZYM acknowledge support from the Research Grants Council of Hong Kong SAR of China (Grant Nos. 17303019, 17301420, 17301721 and AoE/P-701/20), the K. C. Wong Education Foundation (Grant No. GJTD-2020-01), and the Seed Funding “Quantum-Inspired explainable-AI” at the HKU-TCL Joint Research Centre for Artificial Intelligence. YQ acknowledges support from the the National Natural Science Foundation of China (Grant Nos. 11874115 and 12174068). JR is supported by Huawei Young Talents Program at IHES. YCW acknowledges support from the National Natural Science Foundation of China (Grant Nos. 11804383 and 11975024). RS and SS are supported by the U.S. Department of Energy under Grant DE-SC0019030. We thank the Computational Initiative at the Faculty of Science and the Information Technology Services at the University of Hong Kong, and the Tianhe platforms at the National Supercomputer Centers for their technical support and generous allocation of CPU time.

-
- [1] N. Read and S. Sachdev, Phys. Rev. Lett. **66**, 1773 (1991).
[2] X. G. Wen, Phys. Rev. B **44**, 2664 (1991).
[3] R. A. Jalabert and S. Sachdev, Phys. Rev. B **44**, 686 (1991).
[4] X.-G. Wen, Science **363**, eaal3099 (2019).
[5] A. Kitaev, Ann. Phys. **303**, 2 (2003).
[6] S. A. Kivelson, D. S. Rokhsar, and J. P. Sethna, Phys. Rev. B **35**, 8865 (1987).
[7] G. Baskaran and P. W. Anderson, Phys. Rev. B **37**, 580 (1988).
[8] D. S. Rokhsar and S. A. Kivelson, Phys. Rev. Lett. **61**, 2376 (1988).
[9] E. Y. Andrei and A. H. MacDonald, Nat. Mat. **19**, 1265 (2020).
[10] D. M. Kennes, M. Claassen, L. Xian, A. Georges, A. J.

- Millis, J. Hone, C. R. Dean, D. N. Basov, A. N. Pasupathy, and A. Rubio, *Nat. Phys.* **17**, 155 (2021).
- [11] Z. Feng, Z. Li, X. Meng, W. Yi, Y. Wei, J. Zhang, Y.-C. Wang, W. Jiang, Z. Liu, S. Li, F. Liu, J. Luo, S. Li, G. qing Zheng, Z. Y. Meng, J.-W. Mei, and Y. Shi, *Chin. Phys. Lett.* **34**, 077502 (2017).
- [12] X.-G. Wen, *Chin. Phys. Lett.* **34**, 90101 (2017).
- [13] Z. Feng, W. Yi, K. Zhu, Y. Wei, S. Miao, J. Ma, J. Luo, S. Li, Z. Y. Meng, and Y. Shi, *Chin. Phys. Lett.* **36**, 017502 (2018).
- [14] J. J. Wen and Y. S. Lee, *Chin. Phys. Lett.* **36**, 50101 (2019).
- [15] Y. Zhou, K. Kanoda, and T.-K. Ng, *Rev. Mod. Phys.* **89**, 025003 (2017).
- [16] C. Broholm, R. J. Cava, S. A. Kivelson, D. G. Nocera, M. R. Norman, and T. Senthil, *Science* **367**, eaay0668 (2020).
- [17] Y. Da Liao, H. Li, Z. Yan, H.-T. Wei, W. Li, Y. Qi, and Z. Y. Meng, *Phys. Rev. B* **103**, 104416 (2021).
- [18] Z. Zhou, C.-L. Liu, Z. Yan, Y. Chen, and X.-F. Zhang, (2020), arXiv:2010.01750 [cond-mat.str-el].
- [19] R. Samajdar, W. W. Ho, H. Pichler, M. D. Lukin, and S. Sachdev, *Proc. Nat. Acad. Sci.* **118**, e2015785118 (2021).
- [20] R. Verresen, M. D. Lukin, and A. Vishwanath, *Phys. Rev. X* **11**, 031005 (2021).
- [21] G. Semeghini, H. Levine, A. Keesling, S. Ebadi, T. T. Wang, D. Bluvstein, R. Verresen, H. Pichler, M. Kalinowski, R. Samajdar, A. Omran, S. Sachdev, A. Vishwanath, M. Greiner, V. Vuletić, and M. D. Lukin, *Science* **374**, 1242 (2021).
- [22] Z. Yan, R. Samajdar, Y.-C. Wang, S. Sachdev, and Z. Y. Meng, (2022), arXiv:2202.11100 [cond-mat.str-el].
- [23] R. Samajdar, D. G. Joshi, Y. Teng, and S. Sachdev, (2022), arXiv:2204.00632 [cond-mat.quant-gas].
- [24] L. Balents, M. P. A. Fisher, and S. M. Girvin, *Phys. Rev. B* **65**, 224412 (2002).
- [25] S. V. Isakov, R. G. Melko, and M. B. Hastings, *Science* **335**, 193 (2012).
- [26] K. Roychowdhury, S. Bhattacharjee, and F. Pollmann, *Phys. Rev. B* **92**, 075141 (2015).
- [27] X. Plat, F. Alet, S. Capponi, and K. Totsuka, *Phys. Rev. B* **92**, 174402 (2015).
- [28] Y.-C. Wang, C. Fang, M. Cheng, Y. Qi, and Z. Y. Meng, (2017), arXiv:1701.01552 [cond-mat.str-el].
- [29] Y.-C. Wang, X.-F. Zhang, F. Pollmann, M. Cheng, and Z. Y. Meng, *Phys. Rev. Lett.* **121**, 057202 (2018).
- [30] G.-Y. Sun, Y.-C. Wang, C. Fang, Y. Qi, M. Cheng, and Z. Y. Meng, *Phys. Rev. Lett.* **121**, 077201 (2018).
- [31] Y.-C. Wang, M. Cheng, W. Witczak-Krempa, and Z. Y. Meng, *Nat. Commun.* **12**, 5347 (2021).
- [32] Z. Yan, Y.-C. Wang, N. Ma, Y. Qi, and Z. Y. Meng, *npj Quantum Mater.* **6**, 39 (2021).
- [33] S. Sachdev and M. Vojta, *J. Phys. Soc. Jpn.* **69**, Supp. B, 1 (1999), arXiv:cond-mat/9910231.
- [34] R. Moessner and S. L. Sondhi, *Phys. Rev. Lett.* **86**, 1881 (2001).
- [35] R. Moessner, S. L. Sondhi, and P. Chandra, *Phys. Rev. B* **64**, 144416 (2001).
- [36] Z. Zhou, Z. Yan, C. Liu, Y. Chen, and X.-F. Zhang, (2021), arXiv:2106.05518 [cond-mat.str-el].
- [37] D. A. Ivanov, *Phys. Rev. B* **70**, 094430 (2004).
- [38] A. Ralko, M. Ferrero, F. Becca, D. Ivanov, and F. Mila, *Phys. Rev. B* **71**, 224109 (2005).
- [39] G. Misguich and F. Mila, *Phys. Rev. B* **77**, 134421 (2008).
- [40] F. Vernay, A. Ralko, F. Becca, and F. Mila, *Phys. Rev. B* **74**, 054402 (2006).
- [41] A. Ralko, D. Poilblanc, and R. Moessner, *Phys. Rev. Lett.* **100**, 037201 (2008).
- [42] Z. Yan, Z. Zhou, O. F. Syljuåsen, J. Zhang, T. Yuan, J. Lou, and Y. Chen, *Phys. Rev. B* **103**, 094421 (2021).
- [43] Z. Yan, Z. Y. Meng, D. A. Huse, and A. Chan, (2022), arXiv:2204.01740 [cond-mat.str-el].
- [44] Implementation of the sweeping cluster QMC for the two-dimers-per-site constraint, the symmetry analysis of the vison order parameter on the triangular lattice, and the ED results supporting that the VP phase has no symmetry breaking in the dimer densities are presented in the Supplemental Information..
- [45] H. W. J. Blöte and B. Nienhuis, *Phys. Rev. Lett.* **72**, 1372 (1994).
- [46] N. Shannon, G. Misguich, and K. Penc, *Phys. Rev. B* **69**, 220403 (2004).
- [47] L. D. C. Jaubert, M. Haque, and R. Moessner, *Phys. Rev. Lett.* **107**, 177202 (2011).
- [48] Y.-C. Wang, Y. Qi, S. Chen, and Z. Y. Meng, *Phys. Rev. B* **96**, 115160 (2017).
- [49] X.-F. Zhang, Y.-C. He, S. Eggert, R. Moessner, and F. Pollmann, *Phys. Rev. Lett.* **120**, 115702 (2018).
- [50] H. Yao, L. Fu, and X.-L. Qi, (2010), arXiv:1012.4470 [cond-mat.str-el].
- [51] W. Li, S. Yang, M. Cheng, Z.-X. Liu, and H.-H. Tu, *Phys. Rev. B* **89**, 174411 (2014).
- [52] A. Aharony, *Phys. Rev. B* **8**, 4270 (1973).
- [53] M. Hasenbusch and E. Vicari, *Phys. Rev. B* **84**, 125136 (2011).
- [54] L. T. Adzhemyan, E. V. Ivanova, M. V. Kompaniets, A. Kudlis, and A. I. Sokolov, *Nucl. Phys. B* **940**, 332 (2019).
- [55] A. Aharony, O. Entin-Wohlman, and A. Kudlis, (2022), arXiv:2201.08252 [cond-mat.stat-mech].
- [56] A. Pelissetto and E. Vicari, *Phys. Rep.* **368**, 549 (2002).
- [57] S. M. Chester, W. Landry, J. Liu, D. Poland, D. Simmons-Duffin, N. Su, and A. Vichi, *Phys. Rev. D* **104**, 105013 (2021).
- [58] We note the results in Ref. 27 and, in particular, the vanishing of the LN order between $V/t \in (-0.3, 0.7)$, which already points towards the reconciliation.
- [59] Z. Yan, Y. Wu, C. Liu, O. F. Syljuåsen, J. Lou, and Y. Chen, *Phys. Rev. B* **99**, 165135 (2019).
- [60] Z. Yan, “Improved sweeping cluster algorithm for quantum dimer model,” (2021), arXiv:2011.08457 [cond-mat.stat-mech].
- [61] A. Mulder, R. Ganesh, L. Capriotti, and A. Paramekanti, *Phys. Rev. B* **81**, 214419 (2010).
- [62] P. Fendley, K. Sengupta, and S. Sachdev, *Phys. Rev. B* **69**, 075106 (2004).
- [63] H. Bernien, S. Schwartz, A. Keesling, H. Levine, A. Omran, H. Pichler, S. Choi, A. S. Zibrov, M. Endres, M. Greiner, V. Vuletić, and M. D. Lukin, *Nature* **551**, 579 (2017).
- [64] A. Keesling, A. Omran, H. Levine, H. Bernien, H. Pichler, S. Choi, R. Samajdar, S. Schwartz, P. Silvi, S. Sachdev, P. Zoller, M. Endres, M. Greiner, V. Vuletić, and M. D. Lukin, *Nature* **568**, 207 (2019).
- [65] R. Samajdar, W. W. Ho, H. Pichler, M. D. Lukin, and S. Sachdev, *Phys. Rev. Lett.* **124**, 103601 (2020).
- [66] S. Ebadi, T. T. Wang, H. Levine, A. Keesling, G. Se-

- meghini, A. Omran, D. Bluvstein, R. Samajdar, H. Pichler, W. W. Ho, S. Choi, S. Sachdev, M. Greiner, V. Vuletić, and M. D. Lukin, *Nature* **595**, 227 (2021).
- [67] D. Blankschtein, M. Ma, A. N. Berker, G. S. Grest, and C. M. Soukoulis, *Phys. Rev. B* **29**, 5250 (1984).
- [68] D. Blankschtein, M. Ma, and A. N. Berker, *Phys. Rev. B* **30**, 1362 (1984).
- [69] Y. Huh, M. Punk, and S. Sachdev, *Phys. Rev. B* **84**, 094419 (2011).
- [70] K.-A. N. Duerloo, Y. Li, and E. J. Reed, *Nat. Commun.* **5**, 1 (2014).
- [71] Y. Li, K.-A. N. Duerloo, K. Wauson, and E. J. Reed, *Nat. Commun.* **7**, 1 (2016).
- [72] Y. Wang, J. Xiao, H. Zhu, Y. Li, Y. Alsaïd, K. Y. Fong, Y. Zhou, S. Wang, W. Shi, Y. Wang, A. Zettl, E. J. Reed, and X. Zhang, *Nature* **550**, 487 (2017).
- [73] J. Berry, S. Zhou, J. Han, D. J. Srolovitz, and M. P. Haataja, *Phys. Rev. Materials* **2**, 114002 (2018).
- [74] R. Rattazzi, V. S. Rychkov, E. Tonni, and A. Vichi, *JHEP* **2008**, 031 (2008).
- [75] D. Poland, S. Rychkov, and A. Vichi, *Rev. Mod. Phys.* **91**, 015002 (2019).
- [76] M. Campostrini, M. Hasenbusch, A. Pelissetto, P. Rossi, and E. Vicari, *Phys. Rev. B* **65**, 144520 (2002).
- [77] B. Zhao, P. Weinberg, and A. W. Sandvik, *Nat. Phys.* **15**, 678 (2019).
- [78] G. Sun, N. Ma, B. Zhao, A. W. Sandvik, and Z. Y. Meng, *Chin. Phys. B* **30**, 067505 (2021).
- [79] M. Zayed, C. Rüegg, J. Larrea, A. M. Läuchli, C. Panagopoulos, S. S. Saxena, M. Ellerby, D. McMorr, T. Strässle, S. S. Klotz, G. Hamel, R. A. Sadykov, V. Pomjakushin, M. Boehm, M. Jiménez-Ruiz, A. Schneidewin, E. Pomjakushin, M. Stingaciu, K. Conder, and H. M. Rønnow, *Nat. Phys.* **13**, 962 (2017).
- [80] J. Guo, G. Sun, B. Zhao, L. Wang, W. Hong, V. A. Sidorov, N. Ma, Q. Wu, S. Li, Z. Y. Meng, A. W. Sandvik, and L. Sun, *Phys. Rev. Lett.* **124**, 206602 (2020).
- [81] J. L. Jiménez, S. P. G. Crone, E. Fogh, M. E. Zayed, R. Lortz, E. Pomjakushina, K. Conder, A. M. Läuchli, L. Weber, S. Wessel, A. Honecker, B. Normand, C. Rüegg, P. Corboz, H. M. Rønnow, and F. Mila, *Nature* **592**, 370 (2021).
- [82] R. Moessner and S. L. Sondhi, *Phys. Rev. B* **63**, 224401 (2001).
- [83] A. Ralko, M. Ferrero, F. Becca, D. Ivanov, and F. Mila, *Phys. Rev. B* **74**, 134301 (2006).
- [84] A. Ralko, M. Ferrero, F. Becca, D. Ivanov, and F. Mila, *Phys. Rev. B* **76**, 140404 (2007).
- [85] O. F. Syljuåsen, *Phys. Rev. B* **71**, 020401 (2005).
- [86] O. F. Syljuåsen, *Phys. Rev. B* **73**, 245105 (2006).
- [87] O. F. Syljuåsen, *Int. J. Mod. Phys. B* **19**, 1973 (2005).
- [88] O. F. Syljuåsen and A. W. Sandvik, *Phys. Rev. E* **66**, 046701 (2002).
- [89] F. Alet, S. Wessel, and M. Troyer, *Phys. Rev. E* **71**, 036706 (2005).
- [90] F. Alet, J. L. Jacobsen, G. Misguich, V. Pasquier, F. Mila, and M. Troyer, *Phys. Rev. Lett.* **94**, 235702 (2005).

Supplemental Material for “Fully packed quantum loop model on the triangular lattice: Hidden vison plaquette phase and cubic phase transitions”

In this Supplemental Material, we first discuss the derivation of the O(3) vison order parameter and its symmetry transformations (Sec. I). Then, Sec. II illustrates the histograms of the order parameter obtained from QMC simulations, where more details are shown to illustrate the intricate symmetry-breaking patterns in the LN and VP phases. In Sec. III, we discuss the real-space vison correlation function and the real-space kinetic t -term symmetry-breaking pattern of the VP phase. In Sec. IV, the implementation of the sweeping cluster quantum Monte Carlo simulation, with the constraint of two dimers per site, is discussed. Finally, Secs. V and VI present, respectively, the derivations of the QMC measurements of the anisotropy parameters, and the discussion of ED results on a 4×4 system with homogeneous dimer density inside the VP phase and its comparison to QMC.

I. O(3) ORDER PARAMETER

The vison condensation in the quantum loop model on the triangular lattice can be analyzed by mapping it to the ferromagnetic transverse-field Ising model on the dual honeycomb lattice [26, 32, 48, 69], where

$$H_{dual} = J_1 \sum_{\langle IJ \rangle} v_I^z v_J^z + J_2 \sum_{\langle\langle IJ \rangle\rangle} v_I^z v_J^z + J_3 \sum_{\langle\langle\langle IJ \rangle\rangle\rangle} v_I^z v_J^z - \Gamma \sum_I v_I^x. \quad (\text{S1})$$

Here, I and J are the sites on dual lattice while $J_{1,2,3}$ is the first-, second-, and third-neighbor Ising coupling. In the large- Γ limit, all spins point in the x direction. A flipped spin generates a vison excitation, thus $v_I^z = +1(-1)$ is the vison creation (annihilation) operator. As we increase J , the visons acquire a dispersion and eventually condense at its minima. The Fourier transform of the Hamiltonian in Eq. (S1) can be written as

$$H_{dual} = - \sum_{\mathbf{q}} \psi_{\mathbf{q}} J(\mathbf{q}) \psi_{\mathbf{q}}^\dagger, \quad (\text{S2})$$

where $\psi_{\mathbf{q}} = (v_{1q}^z, v_{2q}^z)$, and $J(\mathbf{q})$ is the interaction matrix, which takes the form of

$$J(\mathbf{q}) = \begin{pmatrix} a & b \\ b^* & a \end{pmatrix} \quad (\text{S3})$$

with $J_1 = J_2 = J_3 = 1$. a and b in the above matrix are defined as

$$a = e^{i\mathbf{q}\cdot\mathbf{s}_1} + e^{-i\mathbf{q}\cdot\mathbf{s}_1} + e^{i\mathbf{q}\cdot\mathbf{s}_2} + e^{-i\mathbf{q}\cdot\mathbf{s}_2} + e^{i\mathbf{q}\cdot(\mathbf{s}_1+\mathbf{s}_2)} + e^{i\mathbf{q}\cdot(\mathbf{s}_1-\mathbf{s}_2)}, \quad (\text{S4})$$

$$b = 1 + e^{i\mathbf{q}\cdot\mathbf{s}_1} + e^{i\mathbf{q}\cdot\mathbf{s}_2} + e^{i\mathbf{q}\cdot(\mathbf{s}_1+\mathbf{s}_2)} + e^{-i\mathbf{q}\cdot(\mathbf{s}_1+\mathbf{s}_2)} + e^{i\mathbf{q}\cdot(\mathbf{s}_1-\mathbf{s}_2)}, \quad (\text{S5})$$

where $\mathbf{s}_1 = (\sqrt{3}/2, -3/2)$ and $\mathbf{s}_2 = (\sqrt{3}/2, 3/2)$ are the primitive vectors as shown in Fig. 1(a). The minima of the energy dispersion $J(\mathbf{q})$ occur at three momenta $\mathbf{M}_1 = (\pi/\sqrt{3}, \pi/3)$, $\mathbf{M}_2 = (\pi/\sqrt{3}, -\pi/3)$, and $\mathbf{M}_3 = (0, 2\pi/3)$ in the hexagonal Brillouin zone, as demonstrated in Fig S1. The eigenvectors at these momenta are

$$u_1 = u_2 = (1, 1)^T, \quad u_3 = (1, -1)^T. \quad (\text{S6})$$

Therefore, the vison O(3) order parameter $\phi = (\phi_1, \phi_2, \phi_3)$ can be expressed as

$$\phi_1 = \sum_{\mathbf{r}} (v_{1,\mathbf{r}} + v_{2,\mathbf{r}}) e^{i\pi x}, \quad \phi_2 = \sum_{\mathbf{r}} (v_{1,\mathbf{r}} + v_{2,\mathbf{r}}) e^{i\pi y}, \quad \phi_3 = \sum_{\mathbf{r}} (v_{1,\mathbf{r}} - v_{2,\mathbf{r}}) e^{i\pi(y-x)}, \quad (\text{S7})$$

where x and y are the coordinates of all plaquettes of the triangular lattice.

The O(3) order parameter $\phi = (\phi_1, \phi_2, \phi_3)$ can transform under various symmetries. The transformation matrices for ϕ with respect to translations (T_x, T_y), bond inversion (I), rotation (R_6), global Z_2 , and mirror symmetry M along the y axis, are given by

$$T_x = \begin{pmatrix} -1 & 0 & 0 \\ 0 & 1 & 0 \\ 0 & 0 & -1 \end{pmatrix}, \quad T_y = \begin{pmatrix} 1 & 0 & 0 \\ 0 & -1 & 0 \\ 0 & 0 & -1 \end{pmatrix}, \quad I = \begin{pmatrix} 1 & 0 & 0 \\ 0 & 1 & 0 \\ 0 & 0 & -1 \end{pmatrix}, \quad (\text{S8})$$

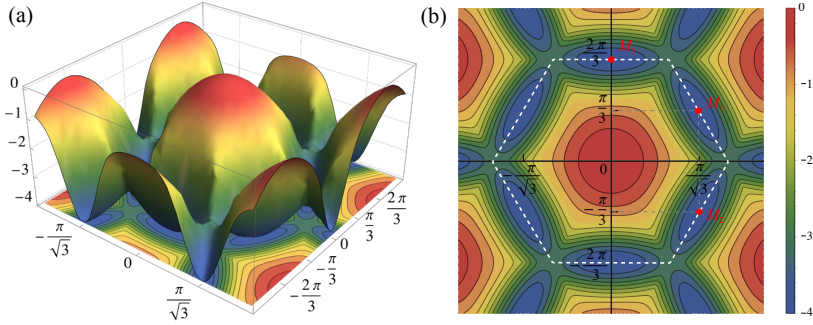


FIG. S1. (a) The dispersion of $J(\mathbf{q})$ and (b) the Brillouin zone (BZ) of the honeycomb lattice. The minima of the energy dispersion $J(\mathbf{q})$ occur at $\mathbf{M}_1 = (\pi/\sqrt{3}, \pi/3)$, $\mathbf{M}_2 = (\pi/\sqrt{3}, -\pi/3)$, $\mathbf{M}_3 = (0, 2\pi/3)$ and the three other symmetry-equivalent \mathbf{M} points.

$$R_6 = \begin{pmatrix} 0 & 0 & -1 \\ 1 & 0 & 0 \\ 0 & 1 & 0 \end{pmatrix}, \quad Z_2 = \begin{pmatrix} -1 & 0 & 0 \\ 0 & -1 & 0 \\ 0 & 0 & -1 \end{pmatrix}, \quad M = \begin{pmatrix} 0 & 0 & -1 \\ 0 & 1 & 0 \\ -1 & 0 & 0 \end{pmatrix}. \quad (\text{S9})$$

These matrices generate a finite subgroup of $O(3)$ which contain 48 elements [26]. This group is isomorphic to $Z_2 \times S_4$, with S_4 being the permutation group of four elements.

II. ORDER PARAMETER HISTOGRAMS

Besides the order parameter histograms presented in the main text, here, we add more detailed results of the evolution from the LN to the VP solid phase. Figure S2 compiles the histograms for a $L = \beta = 16$ system, as V is varied from -1 to 1 . It is clear that for cases with $V < 0.1$, the histograms exhibit the face-cubic distribution, and for the cases with $V > 0.1$, the histograms exhibit the corner-cubic distribution.

Close to the LN-to-VP transition, i.e., the panel with $V = 0.1$ in Fig. S2(b), the histogram develops asymptotic $O(3)$ symmetry with very weak corner-cubic anisotropy (this is because $V = 0.1$ lies on the VP side of the transition). Inside the VP phase, and as V increases towards the VP-QSL continuous transition point $V_c = 0.6$, the histograms [in panels with $V = 0.3, 0.5$ in Fig. S2(b)] begin to shrink in diameters, suggesting the reduction of the vison order parameter. Eventually, inside the QSL phase [panels with $V = 0.7, 0.9$ in Fig. S2(b)], the histogram becomes a point at $(0, 0, 0)$, indicating the complete vanishing of the vison order parameter in the topologically ordered QSL phase.

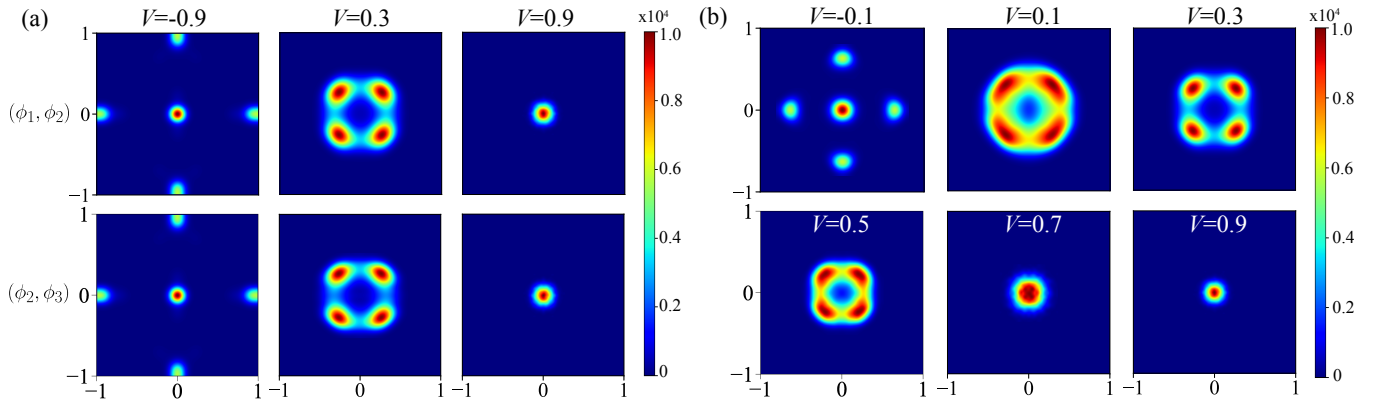


FIG. S2. Order parameter histograms for a $L = 16$ system. (a) Projection of the $O(3)$ order parameter on the (ϕ_1, ϕ_2) plane and (ϕ_2, ϕ_3) plane. The histograms in the three phases (LN with $V = -0.9$, VP with $V = 0.3$, and QSL with $V = 0.9$) are shown. (b) Evolution of the histogram by tuning V , from LN, through VP, to QSL.

III. REAL-SPACE VISON CORRELATIONS

To investigate the symmetry-breaking pattern of the VP phase, the correlations of the triangle- T operators are calculated. As described in the main text, this operator is defined on a triangular plaquette from three related kinetic (t) terms, $T_i = t_{1,i} + t_{2,i} + t_{3,i}$, [see inset of Fig. S3(a)]. Here, i is the triangle label, and 1, 2, 3 connote the three kinds of t -operators (rhombi) in the Hamiltonian acting on this triangle. The correlation of the operators between the triangular plaquettes i and j is $\langle T_i T_j \rangle$.

We calculate the real-space vison correlations with selecting the leftmost and lowest red triangle below as a reference (its correlation is identically 1) as illustrated in Fig. S3(b). Two visons living on the centers of related triangular plaquettes i and j can be connected with a open string; their correlation is $\langle v_i v_j \rangle = \langle (-1)^{N_{P_{ij}}} \rangle$ and $N_{P_{ij}}$ is the number of dimers cut along the path P between plaquettes i and j . In the two-dimer-per-site case, $\langle v_i v_j \rangle$ is independent on the chosen path, i.e., the visons here are gauge invariant and measurable.

We found that the vison correlations clearly exhibit the translational symmetry breaking of the VP solid, but preserve C_3 rotational symmetry. The triangles with positive (negative) values of vison correlations gather into big triangles. In addition, the central triangle of the thus-formed big triangle always has a larger absolute value, which is about three times that of the other triangles in the same big triangle. The translation periods along the \mathbf{s}_1 and \mathbf{s}_2 directions are both 2, which means that the unit cell is a 2×2 rhomboid.

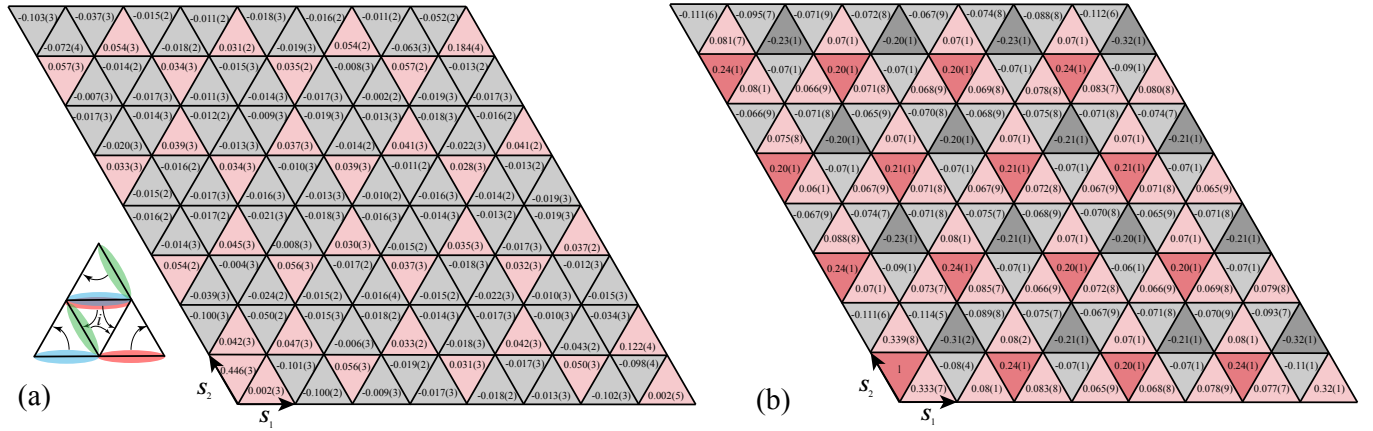


FIG. S3. (a) Real-space T -operator correlations of the $L = 8$ system at $V = 0.3$. The inset shows the summation of the three t terms in the Hamiltonian. (b) Real-space vison correlations of the $L = 8$ system at $V = 0.3$; \mathbf{s}_1 and \mathbf{s}_2 are the primitive vectors. For both figures, we set the leftmost and lowest triangle as the reference. The red (grey) color describes the positive (negative) value of the correlation.

IV. SWEEPING CLUSTER QUANTUM MONTE CARLO WITH TWO DIMERS PER SITE

The sweeping cluster QMC approach employed in this work is a new method developed by us, which works well in constrained quantum lattice models [22, 32, 59, 60]. Prior to sweeping cluster QMC, to solve the QDM or QLM types of constrained models, one had to rely on either exact diagonalization of small systems, or variational approaches such as DMRG that suffer from finite-size effects on the cylindrical geometry [26], or the projector Monte Carlo approaches, which include the Green's function [27, 37, 38, 40, 83, 84] and diffusion Monte Carlo schemes [85, 86]. These projector Monte Carlo methods obey the geometric constraints but are not efficient away from the RK point [87] and only work at $T = 0$. Furthermore, there does not exist any cluster update for the projector methods. On the contrary, the sweeping cluster algorithm is based on the world-line Monte Carlo scheme [88–90] to sweep and update layer by layer along the imaginary time direction so that the local constraints (gauge field) are recorded by update lines. In this way, all the samplings are done in the restricted Hilbert space and it contains the cluster update scheme for constrained systems [60] and works at all temperatures. Proper finite size scaling analysis can then be carried out to explore phase transitions and critical phenomena.

To implement the constraint of having two dimer per site in our QMC simulation, we set the initial state as one of the three LN patters with the same probability [27]. In the region of the LN phase, the equilibrium process will not change the orientation of the initial state; therefore, the randomly selected initial state ensures each pattern of the LN phase has an equal probability of $\frac{1}{3}$ to emerge. In the VP and QSL regions, one can also use such initialization

schemes, and we have tested that in these regions too, they produce the same QMC results as a completely random initialization. We simulate $L \times L$ triangular lattices with system sizes $L = 8, 12, 16$ with the inverse temperature set to $\beta = L$ and 10^4 Monte Carlo samplings used to obtain average values of the observables in all calculations.

In this article, we can measure the information about single visons because in a strictly constrained space, the energy gap of other quasiparticles such as spinons, becomes infinitely large and thus these quasiparticles do not exist in the restricted Hilbert space. Therefore, the vison is well-defined here.

V. ANISOTROPY PARAMETERS

The effective action of the O(3) transition is given by,

$$S = \int dt dx^2 \sum_{i=1}^3 (\partial_\mu \phi_i)^2 + r \sum_{i=1}^3 \phi_i^2 + \mu \left(\sum_{i=1}^3 \phi_i \phi_i \right)^2 + \nu_4 \sum_{i=1}^3 (\phi_i)^4 + \mu_6 \left(\sum_{i=1}^3 \phi_i^2 \right)^3 + \nu_6 (\phi_1 \phi_2 \phi_3)^2 + \nu'_6 \left(\sum_{i=1}^3 \phi_i^2 \right) \left(\sum_{i=1}^3 \phi_i^4 \right). \quad (\text{S10})$$

Assuming that the coupling constants ν_4, ν_6, ν'_6 are all much smaller than one, the average of the spherical harmonics are

$$\begin{aligned} \langle Y_4^0 \rangle &= -\frac{1}{15\sqrt{\pi}} \nu_4 \langle \phi^4 \rangle_0 - \frac{1}{15\sqrt{\pi}} \nu'_6 \langle \phi^6 \rangle_0 - \frac{1}{330\sqrt{\pi}} \nu_6 \langle \phi^6 \rangle_0, \\ \langle \phi^2 Y_4^0 \rangle &= -\frac{1}{15\sqrt{\pi}} \nu_4 \langle \phi^6 \rangle_0 - \frac{1}{15\sqrt{\pi}} \nu'_6 \langle \phi^8 \rangle_0 - \frac{1}{330\sqrt{\pi}} \nu_6 \langle \phi^8 \rangle_0, \\ \langle Y_6^0 \rangle &= -\frac{1}{231\sqrt{13\pi}} \nu_6 \langle \phi^6 \rangle_0. \end{aligned} \quad (\text{S11})$$

Here, $\langle \cdot \rangle_0$ denotes the averages under Boltzmann weights determined by S_0 , where S_0 is the action (S10) with the anisotropic couplings ν_4, ν_6 and ν'_6 turned off. The symbol ϕ denote the length of ϕ_i , i.e., $\phi = (\mu(\sum_{i=1}^3 \phi_i \phi_i)^2)^{1/2}$. The two spherical harmonics are

$$Y_4^0 = \frac{3}{16\sqrt{(\pi)}} (3 - 30 \cos^2 \theta + 35 \cos^4 \theta), \quad (\text{S12})$$

$$Y_6^0 = \frac{\sqrt{13}}{32\sqrt{\pi}} (-5 + 105 \cos^2 \theta - 315 \cos^4 \theta + 231 \cos^6 \theta). \quad (\text{S13})$$

As an example, we explain here how to derive the formula for $\langle Y_4^0 \rangle$:

$$\begin{aligned} \langle Y_4^0 \rangle &= \nu_4 \left\langle Y_4^0 \sum_{i=1}^3 (\phi_i)^4 \right\rangle_0 + \nu_6 \langle Y_4^0 (\phi_1 \phi_2 \phi_3)^2 \rangle_0 + \nu'_6 \left\langle Y_4^0 \left(\sum_{i=1}^3 \phi_i^2 \right) \left(\sum_{i=1}^3 \phi_i^4 \right) \right\rangle_0 \\ &= \nu_4 \langle \phi^4 \rangle_0 \{ Y_4^0 f(\theta, \psi) \}_{S^2} + \nu_6 \langle \phi^6 \rangle_0 \{ Y_4^0 g(\theta, \psi) \}_{S^2} + \nu'_6 \langle \phi^6 \rangle_0 \{ Y_4^0 f(\theta, \psi) \}_{S^2} \\ &= -\frac{1}{15\sqrt{\pi}} \nu_4 \langle \phi^4 \rangle_0 - \frac{1}{15\sqrt{\pi}} \nu'_6 \langle \phi^6 \rangle_0 - \frac{1}{330\sqrt{\pi}} \nu_6 \langle \phi^6 \rangle_0, \end{aligned} \quad (\text{S14})$$

with

$$f(\theta, \psi) = \cos(\theta)^4 + \sin(\theta)^4 \cos(\psi)^4 + \sin(\theta)^4 \sin(\psi)^4, \quad g(\theta, \psi) = \cos(\theta)^2 \sin(\theta)^2 \cos(\psi)^2 \sin(\theta)^2 \sin(\psi)^2. \quad (\text{S15})$$

The bracket $\{A\}_{S^2} = \frac{1}{4\pi} \int A \sin(\theta) d\theta d\psi$ is the average over the unit two-sphere. In the above derivation, we have used the parametrization $\phi_1 = \phi \cos(\theta)$, $\phi_2 = \phi \sin(\theta) \cos(\psi)$ and $\phi_3 = \phi \sin(\theta) \sin(\psi)$. We have also used the approximation $\langle \phi^n f(\theta, \psi) \rangle_0 = \langle \phi^n \rangle_0 \{ f(\theta, \psi) \}_{S^2}$. This crude approximation, strictly speaking, is valid in the semiclassical (approximate mean-field theory) region. The results in Fig. 2 of the main text, however, show that around the first-order phase transition at $V/t = 0.05(5)$, these formulae give reasonable qualitative results for the couplings ν_4, ν_6 and ν'_6 . In particular, ν_4 changes sign at the phase transition as expected.

Through some simple algebra, the three anisotropy parameters can be expressed as

$$\nu_4 = -\frac{15\sqrt{\pi}}{\langle \phi^4 \rangle} \left(\langle Y_4^0 \rangle + \frac{\langle \phi^2 Y_4^0 \rangle \langle \phi^4 \rangle \langle \phi^6 \rangle - \langle Y_4^0 \rangle \langle \phi^6 \rangle^2}{\langle \phi^6 \rangle^2 - \langle \phi^4 \rangle \langle \phi^8 \rangle} \right), \quad (\text{S16})$$

$$\nu_6 = -\frac{231\sqrt{13\pi}}{\langle\phi^6\rangle} \langle Y_6^0 \rangle, \quad (\text{S17})$$

$$\nu'_6 = 15\sqrt{\pi} \left(\frac{\langle \phi^2 Y_4^0 \rangle \langle \phi^4 \rangle - \langle Y_4^0 \rangle \langle \phi^6 \rangle}{\langle \phi^6 \rangle^2 - \langle \phi^4 \rangle \langle \phi^8 \rangle} + \frac{7\sqrt{13}}{10\langle \phi^6 \rangle} \langle Y_6^0 \rangle \right). \quad (\text{S18})$$

We have also used the approximation $\langle \phi^n \rangle_0 = \langle \phi^n \rangle$, which is valid since their difference is of linear order in the perturbation parameters ν_4 , ν_6 , or ν'_6 . These differences only introduce higher-order corrections in Eq. (S11).

VI. EXACT DIAGONALIZATION RESULTS

In this section, we apply the Lanczos exact diagonalization (ED) method to a 4×4 ($N_{bond} = 48$) lattice within the VP phase. The number of configurations of the constrained Hilbert space is 586,695. From the ground state wavefunction, we analyze the wavefunction symmetry of 8 points of cubic order parameters without statistical error. As shown in Fig. S2, the 8 points stay in 8 octants, so each configuration of the wavefunction can be classified into a certain octant, except the ones on the boundaries between different octants. Then—akin to what is done in QMC—we classify configurations according to related octants and average the ones in the same class to obtain the dimer density of a certain cubic order parameter point. It is worth noting that the two classes of opposite octants have opposite sign for vison configurations but their dimer configurations are the same. Thus, we have to average the dimer configurations of the two opposite octants in fact. The result [Fig. S4(a)] is similar to that obtained with QMC: there is still no any dimer order to within the numerical precision of ED. We found that for each link, the real-space dimer density is 1/3.

Similarly, we average the ED vison configurations in each octant. The histogram of the order parameter and the real-space vison density obtained via ED are consistent with our QMC results. The real-space vison density is shown in Fig. S4(b). All these results strongly support the QMC conclusions that there is indeed a hidden vison order phase between the spin liquid and nematic phases.

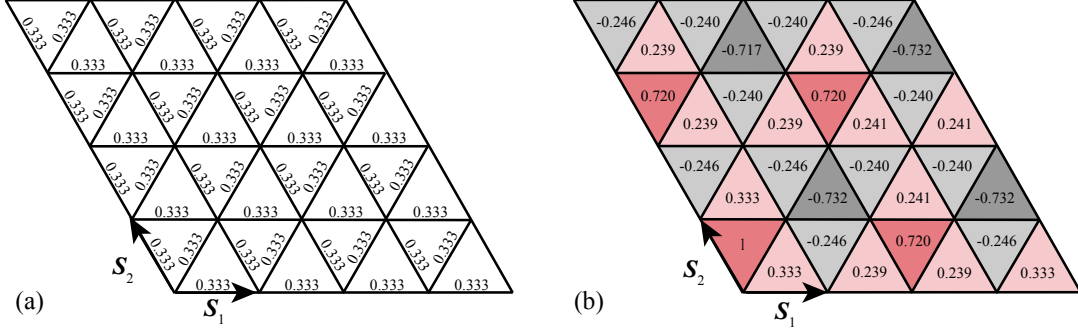


FIG. S4. (a) Exact-diagonalization result for the real-space dimer density for the $L = 4$ system at $V = 0.3$; as previously, \mathbf{s}_1 and \mathbf{s}_2 are the primitive vectors. All bonds hold 1/3 dimer density. (b) The real-space vison density, where we have set $v_1(0,0) = 1$. Similar to the QMC results, four small triangles with the same sign of the vison density form bigger triangles, and the small triangles at the centers of the big ones have a larger absolute value of the density.